UC Berkeley
UC Berkeley Previously Published Works

Title

Dynamic Barriers to Crystallization of Calcium Barium Carbonates

Permalink

https://escholarship.org/uc/item/6bk6g8kq

Journal

Crystal Growth & Design, 21(8)

ISSN

1528-7483

Authors

Whittaker, Michael L
Sun, Wenhao
Duggins, Danielle O
et al.

Publication Date

2021-08-04

DOI

10.1021/acs.cgd.1c00433

Peer reviewed

Dynamic barriers to crystallization of calcium barium carbonates

Michael L. Whittaker,[1][†] Wenhao Sun,[2][††] Danielle O. Duggins,[1] Gerbrand Ceder,[2] Derk Joester[1]*

1. Department of Materials Science and Engineering, Northwestern University, 2220 Campus Dr. Evanston, IL, USA, 60208

2. Materials Sciences Division, Lawrence Berkeley National Laboratory, 1 Cyclotron Rd. Berkeley, CA, USA 94720

ABSTRACT: Metastable carbonates play important roles in geochemistry, biomineralization, and serve as model systems for non-classical theories of nucleation and growth. Balcite ($Ca_{0.5}Ba_{0.5}CO_3$) is a remarkable high-temperature carbonate phase with barium concentrations far greater than the equilibrium solubility limit of calcite, but that can be synthesized in a metastable form at ambient conditions. Here, we investigate crystallization pathways in the Ba-Ca-CO_3-H_2O system, with a focus on the transformation of amorphous calcium barium carbonate (ACBC) to balcite over a range of barium concentrations, and subsequent decomposition into the equilibrium calcite ($CaCO_3$) and witherite ($BaCO_3$) phases. Density functional theory calculations show that balcite is metastable but accessible through the amorphous ACBC precursor for $x \lesssim 0.5$, and predict its decomposition into calcite and witherite. We confirm this pathway experimentally, but found demixing to proceed slowly and remain incomplete even after nine months. Nucleation kinetics of balcite from ACBC were assessed using a microfluidic assay, where increasing barium content led to a surprising increase in nucleation rate, despite decreasing thermodynamic driving force. We attribute crystallization rates that dramatically accelerate with time to changes in interfacial structure and composition during coarsening of the amorphous precipitate. By carefully quantifying the thermodynamic and kinetic contributions in the multistep crystallization of a metastable carbonate, we produce insights that allow us to better interpret the formation and persistence of metastable minerals in natural and synthetic environments.

INTRODUCTION

Metastable phases reside in local energy minima above the ground state, flanked by energy barriers. They provide access to unique properties based on compositions and structures that can be far from equilibrium. Examples abound in nature, where amorphous intermediates are commonly employed by organisms as precursors to the formation of metastable crystalline biominerals.(1) Organisms are thought to use a host of organic macromolecules to guide the crystallization process(2) and have achieved a level of control that remains out of reach for many synthetic systems.

Recently it has been observed that most metastable crystalline phases occupy the relatively narrow range between 5 and 20 kJ/mol above the ground state.(3) An 'amorphous limit' of ~40 kJ/mol appears to establish a hard upper bound of crystalline metastability, above which amorphous states are entropically favored(4) and crystalline phases do not persist.(5) While falling into the metastability window may be a necessary requirement, it does not ensure a metastable phase will form. Favorable kinetics, with barriers below those of other competing phases, are also required.

The barium-calcium-carbonate system is rich in metastable phases. Balcite ($Ca_{0.5}Ba_{0.5}CO_3$) could be synthesized at ambient temperatures as an analog of high temperature 'disordered calcite', with a barium concentration fifty times greater than its equilibrium solubility in calcite ($CaCO_3$).(6) Amorphous calcium barium carbonate (ACBC, $Ca_{1-x}Ba_xCO_3 \cdot 1.2H_2O$) is found to be an important transient intermediate that forms prior to the formation of balcite with composition $x = 0.5$.(7) ACBC with $x > 0.75$ does not reliably crystallize to balcite, and at $x = 1$, a highly transient amorphous barium carbonate (ABC) intermediate(8) converts to witherite via gortatowskite (barium carbonate monohydrate) within milliseconds.(9)

Understanding how the composition of ACBC influences the formation of balcite, or other more ephemeral phases, would yield mechanistic insight into the formation of metastable carbonates.

In contrast to $Ca_{0.5}Mg_{0.5}CO_3$ (dolomite) and $Ba_{0.5}Mg_{0.5}CO_3$ (norsethite), which are stable phases,(10) balcite is not encountered in nature and the thermodynamic status of $Ca_{1-x}Ba_xCO_3$ at ambient temperature has not been measured, e.g., via calorimetry(11, 12). Using density functional theory calculations of solid-state formation energies, supported by long-term bulk crystallization experiments and crystallization assays in confinement, we confirm that all mixed cation phases in the $Ca_{1-x}Ba_xCO_3$ system are metastable or unstable, and show that the theoretically proposed 'metastability window' accurately constrains the range of phases observed. However, we find that barium has a large and counter-intuitive impact on the nucleation rate, which suggests a dominant role for kinetic mechanisms that influence the formation and persistence of metastable carbonates.

Experimental

Consumables

Unless otherwise noted, all aqueous solutions were prepared using ultrapure water (ρ=18.2 MΩ ·cm) from a Barnstead NanoDiamond UF + UV purification unit. Reagent grade (>99%) $BaCl_2 \cdot 2H_2O$, $CaCl_2 \cdot 2H_2O$, $Na_2CO_3 \cdot 2H_2O$, $CaCO_3$, $BaCO_3$, (Sigma-Aldrich), and $(NH_4)_2CO_3$ (ca. 30% NH_3, Alfa Aesar, Haverhill, MA) were used without further purification. Iceland spar calcite was obtained from Dave's Down to Earth Rock Shop in Evanston, IL, USA. Witherite was obtained by the Field Museum of Natural History in Chicago, IL USA (cat #M21424). The fluorous phase for droplet microfluidics was HFE7500 (Novec™ Engineered Fluid, 3M™, St. Paul, MN) containing 2 wt% of a perfluoropolyether-polyethyleneglycol block-copolymer (PFPE-PEG-PFPE) surfactant (008-FluoroSurfactant, RAN Biotechnologies, MA).

1

ACBC and balcite (R$\overline{3}$m) synthesis

We prepared amorphous calcium barium carbonate (ACBC, Ca$_{1-x}$Ba$_x$CO$_3$·nH$_2$O where n $\cong$ 1.2 and 0 < x < 0.5) as described elsewhere.[7] Bulk crystallization of ACBC was initiated by aging at ambient conditions for 24 hours in its mother liquor. The precipitate was then collected by vacuum filtration and dried at 110°C for 1 hour. To establish whether balcite is stable against decomposition into calcite and witherite, 1 g powdered balcite (x = 0.48) was equilibrated with 10 mL Nanopure water and continuously agitated in a rotating mixer at 30 rpm. Samples were removed after three, seven, and nine months, washed with water, and dried in a convection oven at 120°C.

Powder X-ray Diffraction

Diffraction patterns were acquired on a Rigaku Ultima using Cu Kα radiation (λ = 1.504 Å), 0.05° step size, and a sample-to-detector distance of 285 mm.

Raman Microscopy

Approximately 5 mg of dry powder was pressed onto a glass slide for Raman analysis. Raman spectra were obtained on a Horiba LabRam confocal Raman microscope with a laser of wavelength λ = 532 nm, operating at a power of 49 mW, and using a diffraction grating with 1800 g mm−1, resulting in a final spectral resolution of 0.39 cm^{-1}. All spectra were recorded using a 100x objective lens in air (0.9 NA). Mode centers, relative intensities, and full peak width at half maximal intensity (FWHM) were determined by fitting one or more Gaussians to the spectral region of interest. Fitting was performed in Mathematica using custom scripts.

Time-resolved in situ Raman microscopy was performed on droplets stored in wells within a microfluidic device (described below). The device was inverted so that the microfluidic channels and wells were facing away from the objective lens and the optical path of the laser traversed only the glass coverslip substrate and the storage well containing a droplet. Correlated spectra and optical images were collected at regular intervals.

XRF

The mole fractions of barium and calcium were determined on a custom-built X-ray fluorimeter with an Ag-anode operating at 15 mA and 40 kV. Detector calibration was performed using the Fe and Mo Kα lines of a stainless steel ingot of known composition. Background scattering was subtracted from the raw spectra, and corrections for matrix absorption and Compton scattering were applied using XRF-FP v5.2.7 (CrossRoads Scientific). Integrated barium Lα and Ca Kα fluorescence intensity was obtained by fitting Gaussian peak profiles to all calcium and barium fluorescence peaks. The barium cation fraction x was then determined from the barium Lα and calcium Kα fluorescence intensities.

ICP-OES

The barium mole fraction of solutions of the starting materials (x_f) was determined using a Thermo iCAP 7600 instrument. Solutions were diluted 100x in water and then 200x in 3%(v/v) aqueous nitric acid. Intensities for the four strongest emission lines of barium (λ = 230.424, 233.527, 455.403, and 493.409 nm) and Ca (λ=315.887, 393.366, 396.847, and 422.673 nm) were recorded in both axial and radial geometries. Intensities were converted to absolute concentrations using a calibration curve recorded for a series of eight standard solutions ranging from 10 µg/mL to 4 ng/mL that were prepared by serial dilution. An average concentration and standard deviation for barium and calcium was determined from 8 individual values (4 different emission lines in two geometries each).

SEM-EDS

EDS was collected using AZtec software (Oxford Instruments) using an Oxford AZtec X-max 80 SDD EDS detector. Spectra were collected from rectangular areas approximately 5 µm by 5 µm in size within five separate particles and averaged. Data were fit with Gaussian peak profiles and converted to atomic percent using calibrated standards MgO (Mg K-edge 1.0 – 1.4 keV), CaCO3 (Ca K-edge 3.5 – 3.9 keV), and BaTiO3 (Ba L-edges 4.3 –5.7 keV).

Microfluidic nucleation assay

Phase transformations were observed in surfactant-stabilized aqueous droplets dispersed in a fluorous phase. Aqueous feed solutions of BaCl$_2$·2H$_2$O and CaCl$_2$·2H$_2$O with a total cation concentration of approximately 1M were used for droplet production. The barium cation fraction of the feed solution (x_f = [Ba^{2+}]/[Ba^{2+}]+[Ca^{2+}]) was 0.144 $\pm$ 0.001, 0.167 $\pm$ 0.003, 0.255 $\pm$ 0.002, 0.345 $\pm$ 0.008, and 0.534 $\pm$ 0.005, as determined by inductively coupled plasma – optical emission spectrometry (ICP-OES). Droplets (d = 100 µm) were produced using a polydimethylsiloxane (PDMS) microfluidic device with a hydrodynamic flow-focusing geometry.[13] Droplets were collected at the outlet of the flow-focusing device and then loaded into a second device designed to store them in individual wells for imaging. Precipitation was initiated by starting a flow of aqueous (NH$_4$)$_2$CO$_3$ (1.5 M) through channels flanking the droplet storage wells, thereby delivering dissolved gaseous CO$_2$ and NH$_3$.

Experiments were repeated at least two times at each composition. Wells were monitored by time-lapse imaging at a frequency between 1/12 and 1/60 Hz, using a polarized light microscope. Time-lapse movies of all wells were inspected and wells without droplets, multiple droplets, or disruptive events such as droplet fusion were excluded from subsequent analysis. For any given experiment, between 42 and 100 droplets were thus analyzed. The earliest time at which birefringence was detected in any given droplet was recorded as the nucleation time. For droplets with no indication of birefringence at the end of the experiment, the time of the last observation was recorded for right-censoring. Data from all experiments at one concentration (x_f) were combined for analysis. The earliest nucleation time for a given concentration was recorded as the induction time, $\hat{\tau}_i$. The empirical probability density function (PDF, f(t)) and the Kaplan-Meier estimate of the survivor function (SF, S(t)) were determined from the nucleation times for a given experiment. The 95% confidence interval on the survivor function was calculated using Greenwood's formula.[14] The empirical half-life, $\hat{\tau}_{0.5}$, for a given experiment was determined as the time at which the survivor function fell to or below 0.5, which is also the median nucleation time. The confidence interval of the half-life is the percentile bootstrapped interval. PDFs were fit using maximum likelihood estimation with censoring (MLE). For details of model selection and fitting, please refer to the Supporting Information.

DFT simulations

All structures were prepared using the Python Materials Genomic (Pymatgen) package.[15] Specifically 2x2x2 supercells were constructed for R$\overline{3}$c, Pnma, R3m, and R$\overline{3}$m lattices. Vaterite was not considered since uncertainty remains about carbonate order in the structures that have been proposed.[16, 17]

For each structure, a number of cation positions were selected based on the desired composition and the cation on that position was exchanged against the "opposite" cation, i.e. Ca^{2+} for Ba^{2+}, covering the range of x = 0-1 in intervals of Δx = 0.0625. This resulted in 3-10 structural variants at any given composition.

In calcite, Ca2+ is six-fold coordinated by oxygen, whereas in witherite, Ba2+ is nine-fold coordinated by oxygen. To create "disordered" carbonate positions in R$\overline{3}$m structures that retain these coordination numbers, we adopted two procedures to orient carbonate ions to provide favorable coordination. Specifically, carbonates in nearest-neighbor coordination with barium were either sequentially 'flipped', i.e. rotated by 180° about the axis normal to the carbonate plane, or flipping was performed randomly, on one carbonate per barium ion.

All carbonate structures were relaxed in the Vienna Ab-Initio Software Package (VASP) DFT package,[18] using the projector augmented wave (PAW)[19] method with the Perdew–Burke–Erzhenhoff (PBE)[20] generalized-gradient approximation. Plane- wave basis cutoff energies were set at 520 eV for all calculations. Brillouin zones were sampled using Gaussian smearing, with at least 1000 k-points per reciprocal atom. Atoms were initially relaxed until energy differences between ionic steps were 1 meV per atom.

We calculate the Gibbs free energy of the Ca$_{1-x}$Ba$_x$CO$_3$ solid-solution from $\Delta G_{mix} = \Delta H_{mix} - T\Delta S_{mix}$. The ΔH_{mix} is calculated from DFT in the various crystalline structures, and formation enthalpies of the solid-solution are ref-

erenced to calcite and witherite as the end-member reference states. We include the configurational entropy into our calculations of the formation energies with the ideal solution model $S = x \ln x + (1 - x) \ln(1 - x)$, where x is the barium cation fraction at a temperature of 298 K. There is one configurational degree of freedom in the solid-solution for the crystalline $Ca_{1-x}Ba_xCO_3$ solid solutions without carbonate disorder. Calcium/barium disorder on the cation lattice and carbonate orientational disorder on the anion lattice creates two entropic degrees of freedom. The upper bound on the configurational entropy in the cation/anion lattice disordered system is $2 * [x \ln x + (1 - x) \ln(1 - x)]$. We anticipate that the true entropy of the double-disordered lattice is lower than this, as there may be short-range ordering that do not allow both cation and anion sub-lattices to reach full configurational disorder. Formation energies of the solid-solution are referenced to calcite and witherite as end-member reference states.
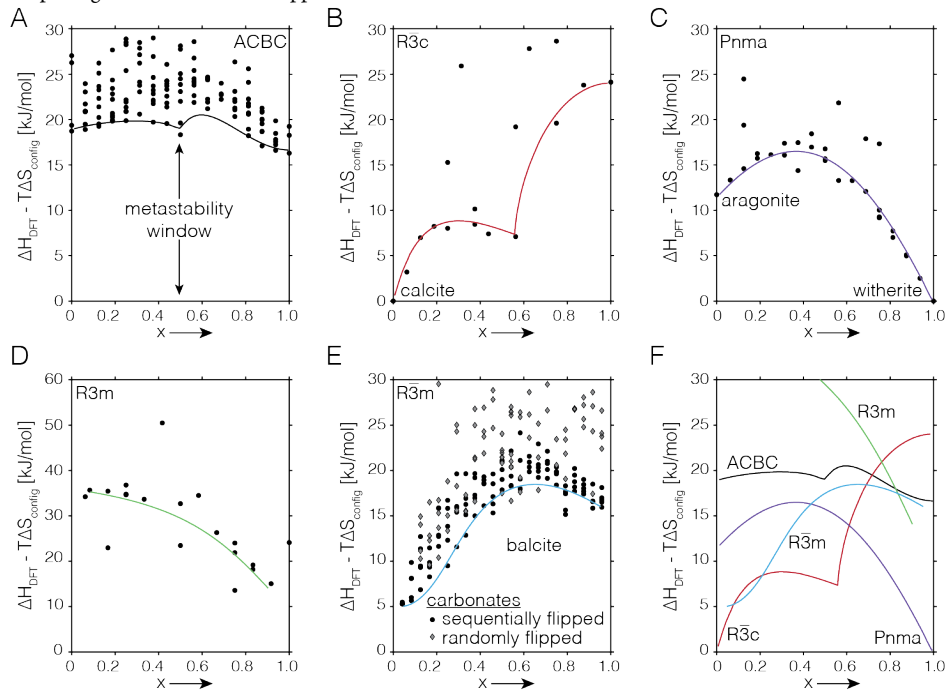

Figure 1. DFT-calculated formation energies (ΔH - $T\Delta S_{config}$) of $Ba_xCa_{1-x}CO_3$. (A) ACBC; (B) calcite ($R\bar{3}c$); (C) aragonite/witherite (Pnma); (D) high-T $BaCO_3$ (R3m); (E) balcite ($R\bar{3}m$); The formation energy of the solid-solution is estimated by approximating the curve that connects the lowest-energy configurations across the $Ba_xCa_{1-x}CO_3$ compositions. (F) Summary of hypothetical free energy curves inferred from DFT data.

RESULTS

Density functional theory (DFT) simulations were used to systematically explore the impact of composition and structure in the $Ba_xCa_{1-x}CO_3$ system. Four structural prototypes were used to generate mixed-cation structures: $R\bar{3}c$ (calcite), Pnma (witherite/aragonite), R3m (high-temperature barium carbonate)(*21*), and $R\bar{3}m$ (balcite) (Figure 1, for crystal structures see Supporting Figure 1). Anhydrous ACBC structures were described previously.(7) Note that the formation energies are reported with respect to the ground state end-members witherite and calcite. We sketch curves that estimate the formation energy of the solid-solution based on the lowest-energy configuration at each composition in $Ba_xCa_{1-x}CO_3$.

The calcite structure ($R\bar{3}c$) quickly becomes less favorable with increasing barium fraction and then plateaus, with a formation energy between 7.5-10 kJ/mol above ground state between $x = 0.13$-0.56. Above $x = 0.56$ it rapidly increases again, climbing beyond 20 kJ/mol at $x = 0.81$, and becoming the least stable phase at the highest barium fractions (**Figure 1A**). The aragonite (Pnma) structure is about 10 kJ/mol higher in energy than calcite at $x = 0$ (**Figure 1B**). Its stability further decreases with increasing barium content (up to $x \approx 0.4$), but then increases. It is the most stable mixed phase above $x = 0.63$, and its formation energy reaches a global minimum at $x = 1$ (witherite).

The lower envelope of the formation energy of ACBC is approximately 20 kJ/mol above this ground state and shows only minor variation with barium content (**Figure 1C**)(7). R3m structures are rather unfavorable, 35 kJ/mol above the ground state in the calcium-rich region (**Figure 1D**) but drop below ACBC structures for compositions above $x = 0.8$. However, these structures are approximately 15 kJ/mol above Pnma structures of the same composition.

The balcite ($R\bar{3}m$) structure lies above the ground state across all compositions (**Figure 1E**). Structures with carbonates flipped randomly and sequentially from the $R\bar{3}m$ space group occupy a similar range of formation energies. However, at low barium content, the latter form the lower bound of the energy envelope. Balcite structures are similar in energy to calcite structures in the range from $x = 0.06$-0.25, but then become less stable, climbing past aragonite at $x = 0.44$ to reach a global maximum near $x = 0.6$. In the range from $x = 0.75$-1, the formation energies of balcite and ACBC are quite similar.

While the approximate envelopes of the free energy data based on the energy of formation plots are qualitative, it appears that the curvature is predominantly negative for all structures, indicating that they are unstable against demixing into Ba-rich and Ba-poor phases (**Figure 1F**). Notable exceptions are calcite and, to a lesser degree, ACBC structures near $x = 0.5$, for which there is a local minimum. For balcite, the curvature is negative in the range $0.3 < x < 0.8$.
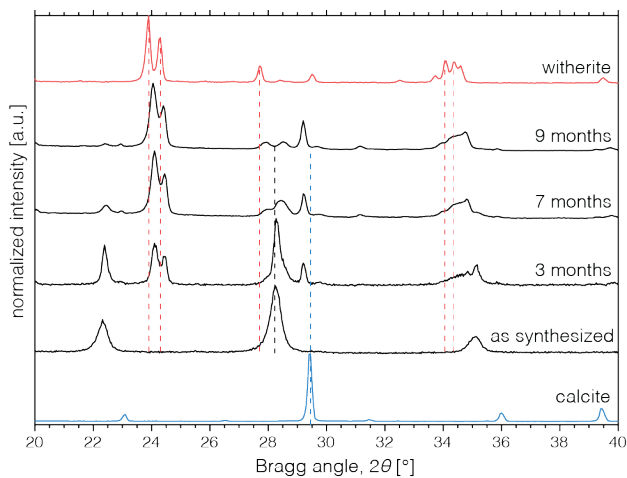
Figure 2. X-Ray diffraction patterns of balcite ($Ba_{0.48}Ca_{0.52}CO_3$) in continuously stirred, aqueous suspension taken over 9 months.

Experimentally, balcite ($x = 0.48$) was observed to phase-separate into calcite and witherite when stirred in a saturated solution (**Figure 2**). Increasing barium content in balcite and calcite causes lattice expansion that shifts diffraction peaks to lower angles. Conversely, increasing calcium content in witherite shifts peaks to higher angles as the lattice contracts. Analysis of XRD patterns of precipitates periodically collected from the same solution revealed that balcite recrystallized into barium-rich calcite and calcium-rich witherite whose compositions became increasingly similar to phase-pure endmembers. The transformation proceeded via balcites with compositions that varied with the extent of the transformation. Complete separation took more than 9 months. We also find that balcite did not form from stirred physical mixtures of calcite and balcite powders, nor of calcite powder mixed with aqueous $BaCl_2$ or witherite mixed with $CaCl_2$, confirming the metastability of balcite relative to calcite and witherite (**Supporting Figure 2**).

A microfluidic nucleation rate assay, recently employed to determine the nucleation rates of vaterite and calcite from amorphous calcium carbonate (ACC),(13) was used to characterize ACBC crystallization (**Figure 3**). Briefly, droplets ($d = 100$ μm) containing an aqueous solution of calcium and barium chlorides were held in a storage chip. Particles formed throughout the droplet volume within one minute after flowing $(NH_4)_2CO_3$ through channels flanking the storage wells. Particles grew, coarsened and coalesced into irregular aggregates over the course of 30 minutes (not shown). Particles initially did not display birefringence and Raman spectra collected from individual droplets in situ were indistinguishable from those of bulk ACBC (**Supporting Figure 3**). The barium cation fraction of ACBC precipitated in droplets, as assessed by in situ Raman spectroscopy, followed similar trends as those in bulk ACBC (**Supporting Figure 4** and **Supporting Table 1**).

Raman spectra acquired *in situ* over 2h indicate that ACBC crystallizes directly to balcite, i.e. without any detectable intermediates (**Supporting Figure 5**). Birefringence appeared at many points, nearly simultaneously, in ACBC-containing droplets and increased in intensity without any appreciable change in overall particle shape detectable by light microscopy, until the entire precipitate appeared bright (**Figure 3A-F**). This contrasts sharply with the crystallization of ACC, where one birefringent particle of vaterite forms per droplet, and then grows at the expense of the amorphous phase with a well-defined exclusion zone indicative of phase transformation by ACC dissolution and reprecipitation (**Figure 3G-L**).(13)

The empirical survivor function, $S(t)$, that quantifies the fraction of droplets that have not crystallized at a given time, t, was strongly impacted by the barium concentration in the feed solution, x_f (**Figure 3M-P** combines trials at the same x_f; see **Supporting Figure 6** for individual trials). The survivor function of ACC displayed a steady but slow decline over time, with an induction time just under five minutes (**Table 1**) and a shallow slope, with 90% of droplets still containing amorphous precipitate at 50 hours (**Figure 3N**). Note that the slope of the natural logarithm of $S(t)$ is identical to the hazard rate, which here is the instantaneous nucleation rate, $J(t)$.

The presence of barium resulted in a survivor function with decreasing sigmoid shape defined by two characteristic time scales, the induction time, $\hat{\tau}_i$, and the half-life, $\hat{\tau}_{0.5}$. At $x_f = 0.14$ the induction time was greater than five hours (**Table 1**). This period with no detectable crystallization events was followed by a period of accelerated crystallization during which the nucleation rate became significantly greater than for ACC and the half-life was 20.4 h. At longer times the rate appeared to level off (**Figure 3O**).

Both the induction time and half-life decreased rapidly with increasing barium fraction for $x_f > 0.14$. Crystallization was greatly accelerated to the point that birefringent particles formed in all droplets in under half an hour from the induction time (**Figure 3P**). Accordingly, half-lives were within 15 minutes of the induction time for these concentrations (**Table 1**).

DISCUSSION

Barytocalcite, alstonite, and paralstonite are crystalline $Ca_xBa_{1-x}CO_3$ minerals with concentrations of $x \sim 0.5$, but balcite has never been documented in the geological record to our knowledge. Combined with observations of rhombohedral structures resembling balcite transforming into barytocalcite at below 525°C(11), it is expected that $Ca_{0.5}Ba_{0.5}CO_3$ is metastable at ambient conditions. Here, we confirmed this using DFT simulations, which reproduce the relative stability of carbonate polymorphs for which structures are known (Figure 1). The $R3\bar{c}$ (calcite) structures are stable at low barium content but become increasingly unfavorable, reaching $\Delta G_f \sim +7.5$ kJ/mol higher in free-energy than the equilibrium mixture of calcite and witherite at the $Ca_{0.5}Ba_{0.5}CO_3$ composition.

It is therefore surprising that we could synthesize crystalline rhombohedral $Ca_{0.5}Ba_{0.5}CO_3$ at ambient conditions. Our DFT-calculated formation energies in Figure 1 illustrate the energetic progression that facilitates the formation of this metastable carbonate. The amorphous ACBC phase plays an essential role in the crystallization sequence, as it forms quickly and is calculated to be metastable by $\Delta G \sim +20$ kJ/mol. Therefore, at the concentration $x = 0.5$, the reaction sequence of supersaturated solution $\rightarrow$ amorphous calcium barium carbonate (ACBC) $\rightarrow$ crystalline $Ca_{0.5}Ba_{0.5}CO_3$ ($R\bar{3}c$) can proceed monotonically downhill in free-energy. Importantly, despite the existence of mineral deposits with heterogeneous mixtures of $CaCO_3$ + $BaCO_3$, there can be no kinetic pathway that would facilitate its uphill transformation to $Ca_{0.5}Ba_{0.5}CO_3$. Altogether, these results emphasize the importance of the crystallization sequence in the formation of metastable minerals—illustrating that their formation is accessible so long as their formation is preceded by an even a higher-energy precursor.

4

Balcite clearly resides within the metastability window for $x \leq 0.5$. The energy gap between balcite and ACBC vanishes at higher barium content and may invert sign at $x = 0.75$. From this and prior studies(22), one would predict that the synthesis of balcite with barium content greater than $x = 0.75$ may be challenging. In our hands, this is indeed the case: we have been unable to synthesize high barium balcite and none has been reported, to our knowledge.

Experimentally, we find that balcite with $x < 0.5$ recrystallizes to phases lower in energy (**Figure 2**), although full transformation took more than 9 months. This indicates that balcite is kinetically persistent, but this should not be confused with balcite being thermodynamically stable.(12) Assessments of thermodynamic stability require experimental calorimetry or *ab initio* calculations, as performed here. Transformation of balcite to calcium-rich witherite and barium-rich calcite occurs through gradual composition changes in all three phases, and therefore lattice parameters, which is reflected in small peak shifts in XRD patterns (**Figure 2**).

Taken together, DFT calculations and experimental evidence clearly support that balcite is a phase that is far from equilibrium, and metastable over a large concentration range. Because the balcite structure has advantageous mechanical properties(6), we systematically explored the impact of composition on its formation from ACBC.

ACBC crystallizes very rapidly in bulk solution, making meaningful comparisons between the rates at different compositions challenging. We therefore turned to a microfluidic crystallization assay (13). The advantage of this assay, as demonstrated for ACC, is that individual nucleation events can be detected and therefore the steady state nucleation rate determined by fitting of time-to-nucleation data.
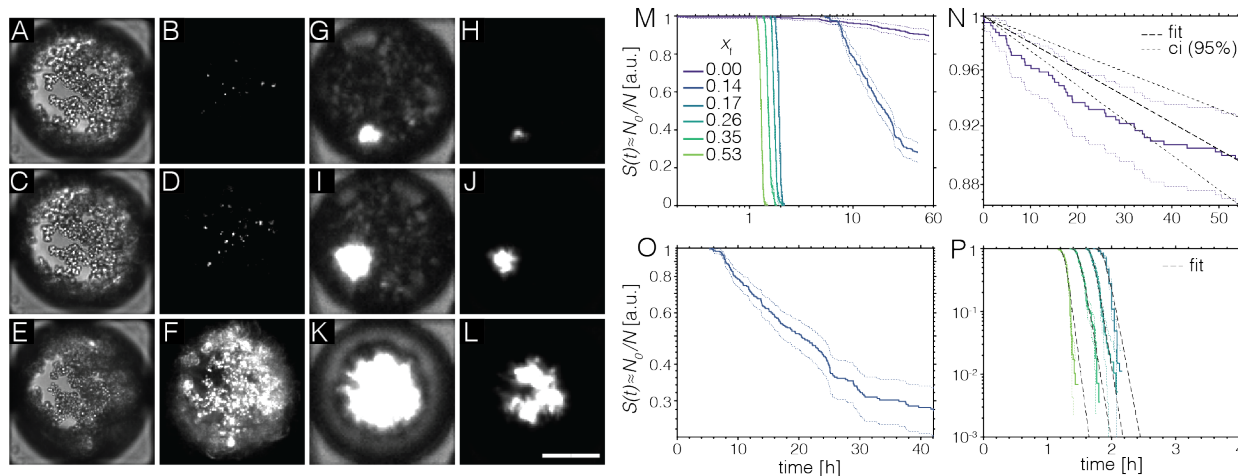

Figure 3. Transformation of ACBC and ACC to balcite in microfluidic droplets. A-F) Images of the same droplet containing ACBC ($x_f = 0.35$) at first appearance of birefringence at 67.75 min (A,B); 68 min (C,D); and 72.5 min (E,F), using bright field (A,C,E) and polarized light contrast (B,D,F). G-L): Images of the same droplet containing ACC ($x_f = 0$) at the first appearance of birefringence at 320 min (G,H); 325 min (I,J); and 370 min (K,L), using polarized light contrast. Note brightness and contrast were adjusted to show non-birefringent ACC in G,I, and K, and, differently, to improve visibility of birefringent particles in B, D, and F. Scalebar represents 40 μm. M) Plot of empirical survivor function versus logarithmic time for ACC ($x_f = 0$) and ACBC with different compositions. Dotted lines indicate 95% confidence intervals. N-P) Plots of empirical survivor function, confidence intervals, and fitted survivor function (black dashed line) against linear time, for ACC (N) and ACBC of different compositions (O,P). Note semi-logarithmic scale for N-P.

Barium has a strong, concentration-dependent effect on the nucleation rate (**Figure 3**). We focused on x_f ~0.14-0.53 because ACBC and balcite can be prepared without secondary phases in this concentration range. The driving force for phase separation into pure calcite and witherite is approximately constant at ~20 kJ/mol (**Figure 1**). Similarly, we expect the driving force for the formation of vaterite to be constant, if somewhat lower. The driving force for the formation of balcite, on the other hand, decreases from ~15 kJ/mol in the absence of barium to near zero at $x = 0.5$. All other things being equal, one would expect the nucleation rate for balcite to decrease significantly compared to that of any of the more stable phases, but we found exactly the opposite to be true.

Qualitatively, this is apparent from a comparison of half-lives that drop by a factor of 260 from $x_f = 0$ to $x_f = 0.53$ (**Table 1**). The largest acceleration, by a factor of ~17 occurs between $x_f = 0$ and $x_f = 0.14$, followed by a factor of ~11 between $x_f = 0.14$ and $x_f = 0.17$. For higher barium concentrations, the reduction in half-life is more moderate, by a factor of ~1.1-1.2 per step.

Interestingly, the very large decrease in half-life from $x_f = 0$ to $x_f = 0.14$ is also associated with a substantial increase in induction time,

by a factor of 67. The induction time is likely to decrease with increasing number of droplets observed in an experiment, simply because events with lower probability are more likely to be observed when the number of observations is higher(23). One should therefore be cautious when interpreting data from experiments with different numbers of droplets. Nevertheless, this dramatic increase clearly indicates that the phase transformation of ACBC to balcite is inhibited at early times, as are the transformations to vaterite and calcite. Curiously, this effect on balcite nucleation is attenuated with increasing barium concentration, and the induction time decreases by a factor of ~3 between $x_f = 0.14$ and $x_f = 0.17$, and between 6% and 16% for each of the following steps.

From the above it is apparent that unlike the steady state nucleation rate for the transformation of ACC to vaterite, the nucleation rate for converting ACBC to balcite is a function of time. Moreover, it is clear that the rate must start very low and increase rapidly in the case where $x_f >= 0.167$. For $x_f = 0.14$ the rate does not increase much beyond 0.1 h⁻¹ and then gradually decreases again by about one order of magnitude over 30 h.

The initial increase in rate most likely means that the reversible work of nucleation, i.e. the nucleation barrier, decreases with time. A linear decrease in nucleation barrier can be modeled using a Gumbel distribution, which is a simplified Gompertz distribution, and is also known as the type-I extreme value distribution for minima. While fitting reproduced the observed half-lives well (not shown), inspection of the fits revealed that the change in nucleation rate in droplets is more rapid than what is predicted by this model.

This is entirely plausible. To the degree that ACBC particles are in metastable equilibrium with the mother liquor, we expect that the supersaturation does not vary much over time, and if anything, decreases. The nucleation barrier is therefore dominated by the interfacial free energy, which enters the reversible work in the third power ($J \propto e^{-W_r^*} \propto e^{-\gamma^3}$), i.e. decidedly non-linear. As there is no reason to assume that the interfacial free energy itself is a linear function of time, choosing a nucleation rate function based on a specific mechanism is difficult. We therefore decided to explore fitting the data with a number of distributions and survival functions commonly used in survival analysis (**Supporting Table 2 and Appendix**) and find that the type-I extreme value distribution for maxima (EV-I max) models the data well for $x_f >= 0.167$ (**Table 1**, **Supporting Table 3**).

The survivor function fit to this model has a rapidly decreasing sigmoidal shape that indicates a rapid onset of nucleation. In fact, the model predicts that less than half an hour is required from the time at which nucleation has occurred in 1% of the droplets to the time where it has occurred in 99% of them, matching our observations well. All of this happens around a time described by the location parameter, $\hat{\mu}$, with the 1% threshold 5-7 minutes earlier and the 99% threshold about 20 minutes later. As the half-life, $\hat{\tau}_{0.5}$, is a function of barium concentration (**Supporting Figure 7**), setting the barium concentration is analogous to setting the length of a fuse or the delay on a timer that switches on crystallization.
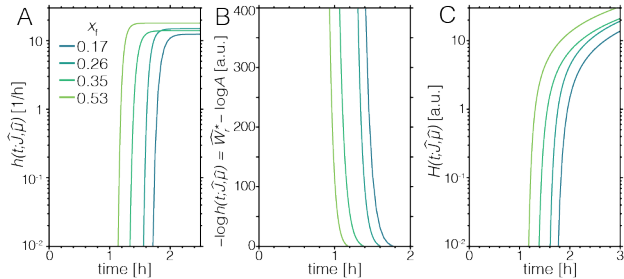

Figure 4. Plot of hazard rate (A), estimate of nucleation barrier (B) and cumulative hazard function (C) vs. time predicted using rate and location parameters of EV-I max distribution fitted to empirical pdf of nucleation times for barium fractions >= 0.167.

The instantaneous nucleation rate (hazard function) EV-I max distribution has the form

$$h(t; \hat{J}, \hat{\mu}) = \frac{\hat{J} e^{-z}}{e^{e^{-z}} - 1}$$

, where $z = \hat{J}(t - \hat{\mu})$, $\hat{J}$ is the (fitted) rate. The hazard function increases exponentially, reaches $\hat{J}/(e-1) \approx 0.58\hat{J}$ at $t = \hat{\mu}$, and then quickly and asymptotically approaches $\hat{J}$ (**Figure 4A**). In the context of nucleation, this implies that the nucleation barrier starts at a rather high value but falls quickly to a constant value briefly after $t = \hat{\mu}$ (**Figure 4B**).

The cumulative hazard for nucleation in a droplet, a measure of the risk that a nucleus will form up to the time of observation, t, assuming no nucleus has yet formed,

$$H(t; \hat{J}, \hat{\mu}) = -\log(1 - e^{-e^{-z}})$$

is about 0.46 at $t = \hat{\mu}$ and reaches 1 within 5 minutes or so after that (**Figure 4C**). This means that multiple nucleation events in a droplet are the expectation rather than the exception. In fact, the assumption that growth is fast compared to nucleation is no longer true. It is thus possible that the observance of birefringence, which requires growth as well as nucleation, is delayed. A systematic overestimation of nucleation times would mean that the true value of μ is smaller than what we report here. Consequently, the cumulative hazard at the time that we identified as the half-life may be even higher, with $\hat{J}$ nuclei formed in a droplet within one hour of passing $t = \hat{\mu}$, on average. It is likely that this is the reason for the nearly simultaneous development of birefringence in many ACBC particles within the same droplets.

If the time-dependence of the nucleation rate is the result of a time-dependent interfacial free energy, then the interface most likely to change with time is that between ACBC particles and bulk solution. One possible mechanism is that the interfacial structure of ACBC becomes more similar to balcite. We previously observed that the local order of ACBC and balcite becomes more similar as the barium fraction increases (6). In our calculations, we found in Figure 1E that cation coordination has a dominant influence over phase stability. Calcite has monodentate carbonate coordination to cations, while both Pnma and R3m structures offer 9-fold barium coordination through a mixture of mono- and bi-dentate coordination. The favorability of structures with 9-fold coordination at high barium content is consistent with the preference of barium for higher coordination numbers. It is therefore plausible that a cation coordination that is favorable for the crystalline phase appears in the amorphous precursor at high Ba^{2+} concentrations in ACBC.

Other changes in the interfacial structure might result from compositional changes at the interface, which include loss of water from ACBC similar to the dehydration of ACC (7) and the adsorption and/or incorporation of ions (such as excess Ba^{2+}) from the mother liquor. Such compositional changes are expected during coarsening, a process that one can assume to be active in the droplets. In this model, a lower initial barium concentration means not only that the interface would have to undergo greater change in composition to adopt balcite-like structure, but that it would have to do so with a smaller excess in the mother liquor. This is consistent with both induction times and half-lives that decrease with increasing barium concentration in microfluidic assays (**Figure 4**). However, it is not possible to unequivocally rule out other mechanisms based on the data presented herein.

We have previously observed that ACC particles coarsen, (13) i.e. that larger particles grow at the expense of smaller ones. In addition to altering the interfacial composition (24), coarsening may also create topographical features such as pits or crevices that lower the nucleation barrier. For example, coarsening of aggregated of spherical ACBC particles may result in circular wedge-shaped crevices surrounding the contact point.

We note that the apparent slow-down of the rate at $x_f = 0.14$ is not easily explained by our model. It may be that this composition straddles the boundary below which Raman spectra and XRD patterns are calcite-like and vaterite appears as a co-precipitate, and above which Raman spectra are consistent with balcite and no secondary phases are observed (7, 12). This composition coincides with the location of the binodal in the $R\bar{3}m$ free energy curve (**Figure 1**) and is likely the result of competition by cations for oxygen coordination. Cations have six next-nearest cation neighbors in both the calcite and the

balcite lattice, such that the minimum barium percolation threshold (i.e., each barium has at least one barium cation-nearest-neighbor) is $x = 1/6 \cong 0.17$. Percolation of barium throughout the cation lattice destabilizes the $R\bar{3}c$ structure via the disordering of carbonates(7), favoring the formation balcite. At $x_f = 0.14$, some ACBC precipitates may have barium contents approaching $x_f = 0.17$ which promote the formation of balcite, while others may not (**Supporting Figure 4, Supporting Table 1**). Experiments with a larger number of droplets would help constrain the fitting, and systematic variation of the temperature would enable a better estimate of the height of the barrier. Unlike the case of ACC, where crystallization is slow and observations in small volumes become impractical, it might be possible to use cryo-electron microscopy to determine crystallization rates of ACBC in liposomes(25).

CONCLUSIONS

Crystalline $Ca_xBa_xCO_3$ phases within ~20 kJ/mol above the ground state were synthesized in this study across the entire range of compositions. The value of 20 kJ/mol is commensurate with the energy of the amorphous calcium barium carbonate phase, which is wholly consistent with theoretical assertion that a narrow 'metastability window' for crystalline materials is constrained by the energy of the amorphous phase. Not only does the amorphous phase determine which balcite compositions can form, ACBC also serves as an important intermediate phase in the balcite crystallization pathway, offering a stepwise reaction that is monotonically decreasing in energy. The amorphous phase therefore affords the formation of metastable balcite $Ca_xBa_xCO_3$ with barium concentrations that are 50x beyond the equilibrium solubility limit. In confinement, the half-life of ACBC strongly depends on the barium concentration. With a dramatic, barium-dependent rate increase over a short period of time, the timing of the transformation becomes tunable. This is likely due to processes that decrease the ACBC-water interfacial energy, including emergent structural similarity between precursor and product, dehydration, compositional changes during coarsening, and/or changes in the topography of the interface. The ability to precisely control the onset of nucleation is especially important in confinement, where steady state nucleation would otherwise result in a wide spread of transformation half-lives and no control over induction time. In biomineralizing organisms, this level of control is generally thought to involve bio-macromolecules. We have shown here that inorganic components may play an equally important role.

Table 1: Crystallization kinetics

x_f	Number of droplets, N	Product	Induction time, $\hat{\tau}_i$ [h]	Half-life, $\hat{\tau}_{0.5}$ (95% CI) [h]	Model	Rate, $\hat{J}$ (95% CI) [h⁻¹]	Location, $\hat{u}$ (95% CI) [h]
0	404	vaterite	0.08	338* (260-485)*	Exponential	2.05·10⁻³ (1.43-2.67)·10⁻³	- -
0.144	285	balcite	5.33	20.42 (16.92-23.42)			
0.167	267	balcite	1.71	1.92 (1.92-1.96)	EV-1 (max)	12.44 (11.37-13.50)	1.891 (1.881-1.901)
0.255	191	balcite	1.6	1.75 (1.72-1.75)	EV-1 (max)	14.92 (13.25-16.59)	1.710 (1.700-1.720)
0.345	278	balcite	1.35	1.52 (1.52-1.53)	EV-1 (max)	13.98 (12.72-15.24)	1.496 (1.487-1.505)
0.534	290	balcite	1.17	1.30 (1.29-1.30)	EV-1 (max)	18.03 (16.53-19.53)	1.266 (1.259-1.273)

*Predicted based on fitted rate expression.

ASSOCIATED CONTENT

Supporting Information

The Supporting Information is available free of charge on the ACS Publications website.

Supporting_Information.pdf: Structural models; XRD patterns; Raman spectra; compositional measurements; nucleation assay data, model selection and fitting.

AUTHOR INFORMATION

Corresponding Author

* Prof. Derk Joester: d-joester@northwestern.edu

Present Addresses

† Energy Geoscience Division, Lawrence Berkeley National Laboratory, 1 Cyclotron Rd, Berkeley CA 94720
†† Department of Materials Science and Engineering, University of Michigan, 2300 Hayward St, Ann Arbor MI 48109

REFERENCES

1.   J. J. De Yoreo *et al.*, CRYSTAL GROWTH. Crystallization by particle attachment in synthetic, biogenic, and geologic environments. *Science* **349**, aaa6760 (2015).

2.   J. E. Saal, S. Kirklin, M. Aykol, B. Meredig, C. Wolverton, Materials Design and Discovery with High-Throughput Density Functional Theory: The Open Quantum Materials Database (OQMD). *Jom* **65**, 1501-1509 (2013).

3.   W. Sun *et al.*, The thermodynamic scale of inorganic crystalline metastability. *Science Advances* **2**, e1600225 (2016).

4.   M. Aykol, S. S. Dwaraknath, W. Sun, K. A. Persson, Thermodyamic limit for synthesis of metastable inorganic materials. *Science Advances* **4**, eaaq0148 (2018).

5.   W. L. Johnson, Crystal-to-glass transformation in metallic materials. *Materials Science and Engineering* **97**, 1-13 (1988).

6.   M. L. Whittaker, D. Joester, ACBC to Balcite: Bioinspired Synthesis of a Highly Substituted High-Temperature Phase from an Amorphous Precursor. *Adv Mater* **29**, (2017).

7.   M. L. Whittaker *et al.*, Structural basis for metastability in amorphous barium calcium carbonate. *Advanced Functional Materials*, (2017).

8.   S. Leukel, M. Mondeshki, W. Tremel, Hydrogen Bonding in Amorphous Alkaline Earth Carbonates. *Inorg Chem* **57**, 11289-11298 (2018).

9.   M. L. Whittaker, P. J. Smeets, H. Asayesh-Ardakani, R. Shahbazian-Yassar, D. Joester, Multi-step crystallization of barium carbonate: rapid interconversion of amorphous and crystalline precursors. *Angew Chem Int Ed Engl* **In Press**, (2017).

10.   C. Pimentel, C. M. Pina, The formation of the dolomite-analogue norsethite: Reaction pathway and cation ordering. *Geochimica et Cosmochimica Acta* **142**, 217-223 (2014).

11.   L. L. Chang, Subsolidus phase relations in the systems BaCO3-SrCO3, SrCO3-CaCO3, BaCO3-CaCO3. *The Journal of Geology* **73**, 346-368 (1965).

12.   E. Seknazi, D. Levy, I. Polishchuk, A. Katsman, B. Pokroy, Experimental and Theoretical Insights into the Bioinspired Formation of Disordered Ba-Calcite. *Advanced Functional Materials*, 1805028.

13.   J. Cavanaugh, M. L. Whittaker, D. Joester, Crystallization kinetics of amorphous calcium carbonate in confinement. *Chemical Science* **10**, 5039-5043 (2019).

14.   MATLAB. (The MathWorks Inc., Natick, Massachusetts, 2019).

15.   S. P. Ong *et al.*, Python Materials Genomics (pymatgen): A robust, open-source python library for materials analysis. *Computational Materials Science* **68**, 314-319 (2013).

16.   L. Kabalah-Amitai *et al.*, Vaterite crystals contain two interspersed crystal structures. *Science* **340**, 454-457 (2013).

17.   R. Demichelis, P. Raiteri, J. D. Gale, R. Dovesi, A new structural model for disorder in vaterite from first-principles calculations. *CrystEngComm* **14**, 44-47 (2012).

18.   G. Kresse, J. Furthmüller, Efficient interative schemes for ab initio total-energy calculations using a plane-wave basis set. *Physical Review B* **54**, 11169 (1996).

19.   G. Kresse, From ultrasolf pseudopotentials to the projector augmented-wave method. *Physical Review B* **59**, 1758 (D Joubert).

20.   J. P. Perdew, K. Burke, M. Ernzerhof, Generalized Gradient Approximation Made Simple. *Physical Review Letters* **77**, 3865 (1996).

21.   S. M. Antao, I. Hassan, BaCO3: high-temperature crystal structures and the Pmcn -> R3m phase transition at 811 degrees C. *Phys Chem Miner* **34**, 573-580 (2007).

22.   J. Terada, Crystal structure of the Ba, Sr, and Ca triple carbonate. *Journal of the Physical Society of Japan* **8**, 158-164 (1953).

23.   W. Sun, G. Ceder, Induction time of a polymorphic transformation. *CrystEngComm* **19**, 4576 (2017).

24.   T. Philippe, P. W. Voorhees, Ostwald ripening in multicomponent alloys. *Acta Materialia* **61**, 4237-4244 (2013).

25.   C. C. Tester, D. Joester, Precipitation in liposomes as a model for intracellular biomineralization. *Methods Enzymol* **532**, 257-276 (2013).
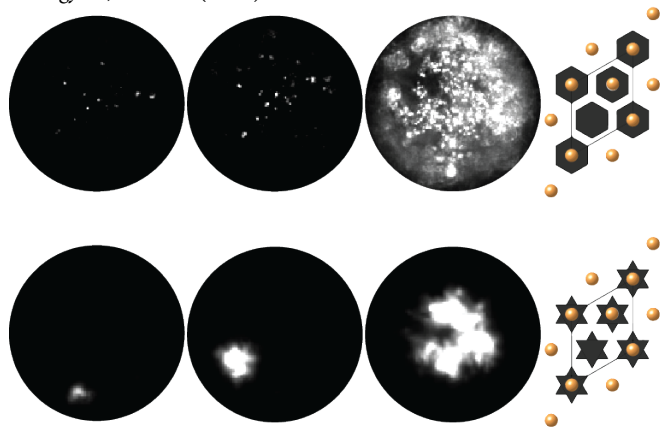
Insert Table of Contents artwork here

SUPPORTING INFORMATION

1   Supporting Figure of Structure Models
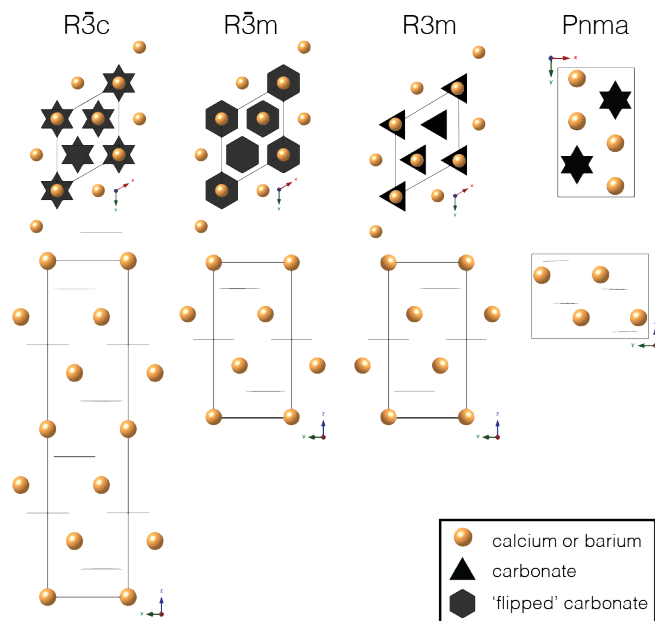
Supporting Figure 1. Carbonate structures used for DFT models. Schematic rendering of the calcite ($R\bar{3}c$), balcite ($R\bar{3}m$), high-T $BaCO_3$ (R3m), and aragonite/witherite (*Pnma*) structures viewed along the $[001]$ direction (top row) and the $[100]$ direction (bottom row). Two additional $Ca_{0.5}Ba_{0.5}CO_3$ polymorphs, alstonite and paralstonite, are not depicted because their structures and compositions are not known with certainty,(*25*) but are expected to be metastable at $x = 0.5$. Barytocalcite is also expected to be slightly metastable with respect to witherite and calcite,(*26*) and more stable than $R\bar{3}m$ structures.(*11*)

2   Balcite Stability
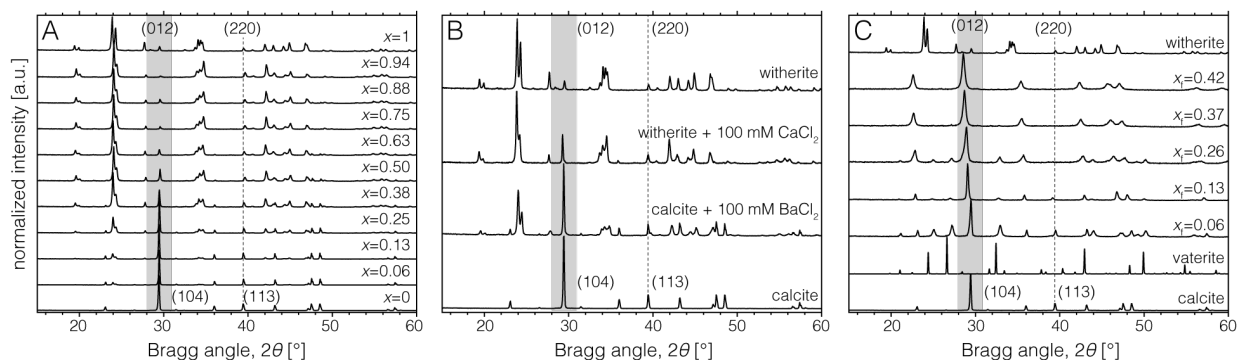
Supporting Figure 2. A) Powder XRD patterns of physical mixtures of calcite and witherite powders with nominal composition $Ca_{1-x}Ba_xCO_3$ that were suspended in water and stirred continuously at room temperature for 30 days. Note that the calcite (104) and (113) and the witherite (012) and (220) reflections only vary in intensity, not in position or width. In balcites, the (104) reflection is shifted to lower angle and broadened, and the (113) reflection disappears, as seen in (C). B) Powder XRD patterns of witherite powder suspended in an aqueous solution of $CaCl_2$ ($100\,mM$) and of calcite powder suspended in an aqueous solution of $BaCl_2$ ($100\,mM$), after stirring continuously at room temperature for 30 days. Again, there is no indication that balcite formed under these conditions. C) X-ray diffraction patterns recorded after aging ACBC for 24 hours in the mother liquor show shift of (104) reflection towards lower angle, broadening, and loss of the (113) reflection typical for balcite formation.

3 Characterization of ACBC and Balcite in Bulk and Microfluidic Droplets

3.1 Bulk and in situ Raman spectra of ACBC and balcite in microfluidic droplets and reference materials
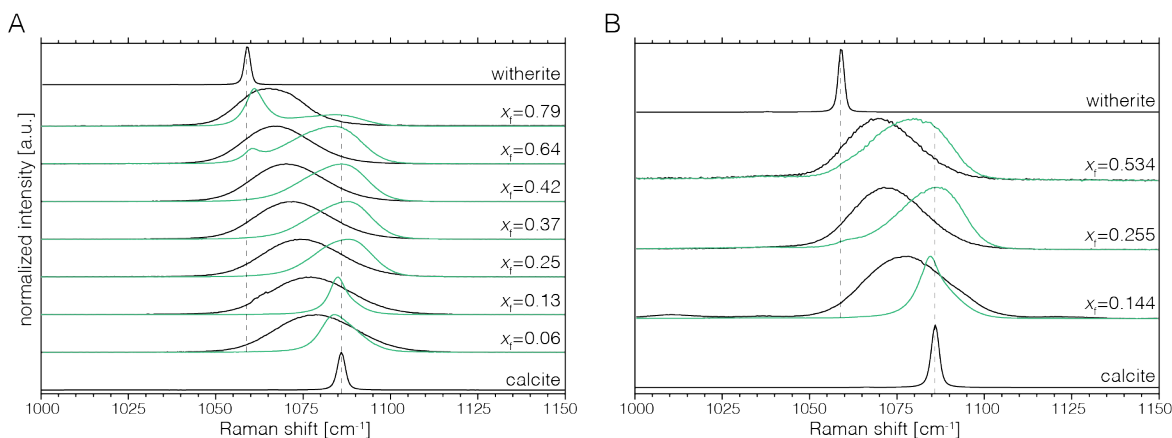
Supporting Figure 3. Partial Raman spectra of ACBC and its transformation to balcite in bulk (A) and in microfluidic droplets (B). Spectra region near the ν_1 mode of calcite and witherite for ACBC (black) precipitated from feed solutions with barium cation fraction x_f, and of balcite precipitates obtained by aging of ACBC in the mother liquor for 24 h at room temperature (green). The position of the ν_1 mode of pure witherite and calcite is indicated (dashed lines).

3.2 ACBC and Balcite Precipitate Composition
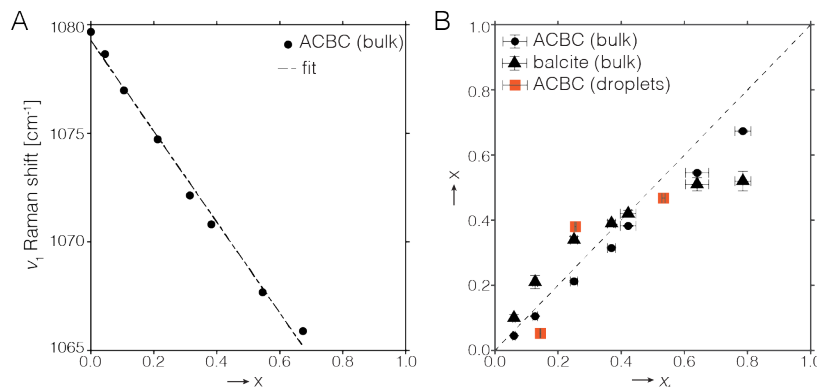
Supporting Figure 4. A) Plot of position of Raman ν_1 mode of bulk ACBC (see Supporting Figure 3) as a function of the barium cation fraction, x, as assessed by XRF, and a linear model fitted to the data (dashed line, $y/\text{cm}^{-1} = -20.92x + 1079.3$, $R^2 = 0.992$). B) Plot of the barium cation fraction, x, of bulk ACBC, assessed by XRF, as a function of the barium cation fraction of the feed solution, x_f, assessed by ICP-OES (solid circles, from ref (6)); plot of barium cation fraction of bulk balcite obtained after aging ACBC in the mother liquor for 24 h at room temperature, x, assessed by SEM-EDS, as a function of the barium cation fraction of the feed solution, x_f (solid triangles); plot of barium cation fraction of ACBC in droplets, determined using Raman ν_1 mode position and linear model in (A), as a function of the barium cation fraction of the feed solution, x_f (red squares). The dashed line indicates $x = x_f$.

| Supporting Table 1: Composition, x, of feed solution and the resulting ACBC and balcite precipitates.					
Feed solution: ICP-OES		**Bulk ACBC: XRF**		**Bulk Balcite: SEM-EDS**	
x_f	std. dev.	x	std. dev.	x	std. dev.
0		0		0	-
0.060	0.0035	0.045	0.001	0.10	0.01
0.127	0.0073	0.105	0.001	0.21	0.02
0.251	0.0116	0.212	0.002	0.34	0.01
0.369	0.0127	0.314	0.003	0.39	0.01
0.422	0.0248	0.382	0.002	0.42	0.01
0.640	0.0370	0.545	0.003	0.51	0.02
0.785	0.0254	0.673	0.004	0.52	0.03

10

3.3 Time resolved Raman spectra of phase transformation from ACBC to balcite and witherite in confinement
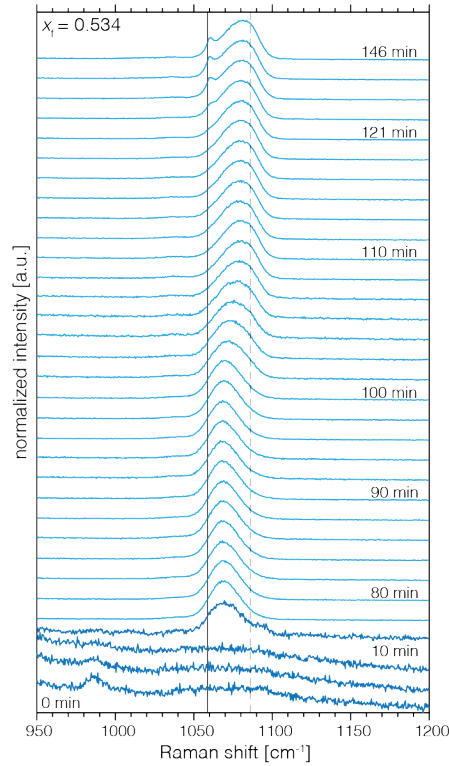
Supporting Figure 5. *In situ* Raman spectra of ACBC precipitation in a single microfluidic droplet (dark blue lines) and of conversion of ACBC to balcite and eventual precipitation of witherite in a different droplet (light blue lines) of the same experiment. Only the spectral region near the ν_1 mode is shown. The position of the witherite (solid black line) and calcite (dashed black line) ν_1 modes are indicated.

4 Droplet Crystallization Assay

4.1 Raw data
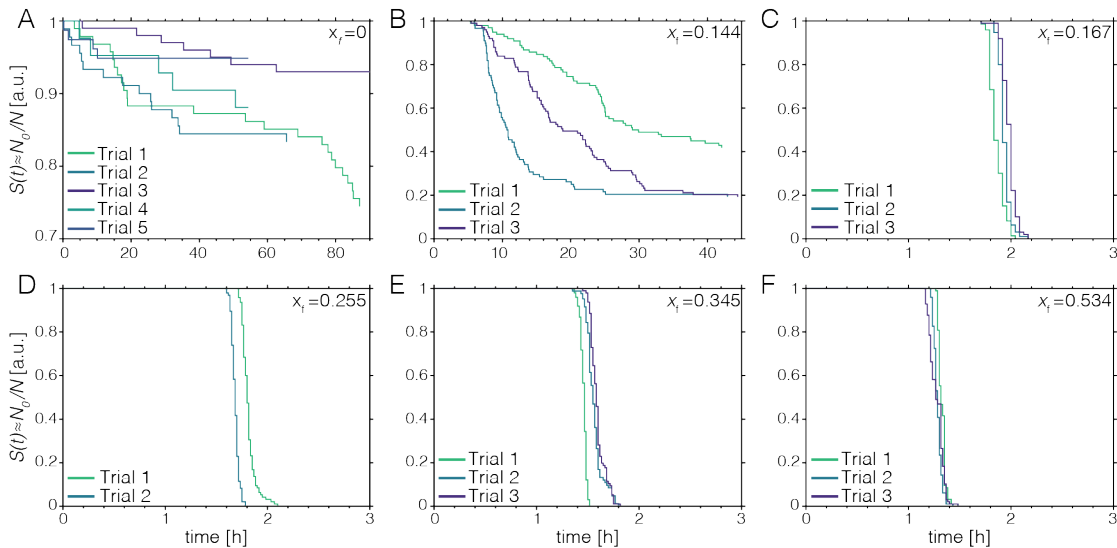
Supporting Figure 6. Microfluidic nucleation rate assays for the crystallization of ACC (A) and ACBC at different barium cation fractions in the feed solution (B-F). The survival time, i.e. the time at which birefringence was first detected in each droplet, was recorded and the cumulative distribution of survival times (survival function) for individual experimental trials are plotted here. Empirical survival functions reported in **Figure 3** were generated by combining trials for a given barium cation fraction.

4.2 Model Selection for Droplet Crystallization Data

4.2.1 Approach

Crystallization data for ACC ($x_f = 0$) were fit assuming a steady state (constant) nucleation rate, as previously described.[27] For all other experiments, we assumed that the instantaneous rate was time dependent. For $x_f = 0.144$, the behavior is complex, with an acceleration of the rate followed by a deceleration that left a considerable fraction of droplets without crystals at the end of the experiment. We were unable to find a satisfactory model for this case. For experiments where $x_f \geq 0.167$ M, there is a clear increase in the nucleation rate over time. This is a less common observation in nucleation experiments.[28] For these experiments, we considered mechanistic and more general models that are commonly used in survival analysis.

An increasing nucleation rate is an expected feature for systems described by classical nucleation theory where the reversible work of nucleation, i.e. the nucleation barrier, decreases with time. Postulating that this decrease in the barrier is a linear function of time, one can show that the probability density function of survival times is a Gompertz distribution. The Gompertz distribution has parameters J_0, the initial nucleation rate at $t = 0$, and $\widehat{W}'$, the constant rate of change of the nucleation barrier (**Appendix** and **Supporting Table 2**). When the initial rate is much smaller than the rate by which the barrier decreases, the Gompertz distribution simplifies to a Gumbel distribution with the same parameters (**Appendix** and **Supporting Table 2**). The Gumbel distribution is identical to the type-1 extreme value distribution for minima (EV-I (min)). Extreme value distributions have found application in analysis of ice nucleation.[29-32] The generalized extreme value (GEV) distribution encompasses the 3 families of distributions (Type 1, 2, and 3). The GEV distribution is a 3-parameter distribution and the shape parameter, k, determines the Type (**Appendix** and **Supporting Table 2**).

Distribution	PDF, $f(t)$	Survivor Function, $S(t)$	Hazard Function, $h(t)$	z
Gompertz	$J_0 \exp\left(\frac{-J_0}{\widehat{W}'}\left(1 - e^{\widehat{W}'t}\right)\right) e^{-\widehat{W}'t}$	$\exp\left(-\frac{J_0}{\widehat{W}'}\left(1 - e^{-\widehat{W}'t}\right)\right)$	$J_0 e^{-\widehat{W}'t}$	N/A
Gumbel	$J_0 \exp\left(-\widehat{W}'t + \frac{J_0}{\widehat{W}'}e^{-\widehat{W}'t}\right)$	$\exp\left(\frac{J_0}{\widehat{W}'}e^{-\widehat{W}'t}\right)$	$J_0 e^{-\widehat{W}'t}$	N/A
GEV, for $k \neq 0$ & $kz > -1$	$J(1+kz)^{\left(-1-\frac{1}{k}\right)} \exp\left(-(1+kz)^{-\frac{1}{k}}\right)$	$1 - \exp\left(-(1+kz)^{-\frac{1}{k}}\right)$	$\dfrac{J(1+kz)^{\left(-1-\frac{1}{k}\right)}}{\exp\left(-(1+kz)^{-\frac{1}{k}}\right)-1}$	$z = J(t-\mu)$
GEV, for $k = 0$ & EV-1 (max)	$Je^{-z-e^{-z}}$	$1 - e^{-e^{-z}}$	$\dfrac{Je^{-z}}{\exp(e^{-z})-1}$	$z = J(t-\mu)$
EV-1 (min)	$Je^{z-e^{z}}$	$e^{-e^{z}}$	Je^{z}	$z = J(t-\mu)$

Supporting Table 2. Equations for probability density and survivor functions of models used in model selection.

4.3 Fitting

Gompertz, Gumbel, and GEV models were fit to the probability density of the empirical survival times using maximum likelihood estimation (MLE) implemented in Matlab.[14] To compare between models with different numbers of parameters, we used the Akaike information criterion (AIC) as a measure of the goodness of fit, g^{AIC}.[33] This criterion is defined as

$$g^{AIC} = -2\log\mathcal{L}\left(\hat{\theta}\middle|y\right) + 2K$$

where $\mathcal{L}\left(\hat{\theta}\middle|y\right)$ is the likelihood function of the observed outcome, y, given the fit parameters, $\hat{\theta}$, and K is the number of parameters.[33] Models with the lowest g^{AIC} values are considered the most probable. Because g^{AIC} values are subjective for a given dataset, the differences, $\Delta g_i^{AIC} = g_i^{AIC} - \min\{g^{AIC}\}$, are often reported instead of the absolute values. Models with small Δg_i^{AIC} values (<2) should be kept as candidate models, while models with $\Delta g_i^{AIC} > 10$ are unlikely to be an accurate model for the system.[33] Goodness of fit data are reported in **Supporting Table 3**.

The GEV distribution was found to be by far the best fit for each of the datasets. The GEV shape parameter, k, determines which type of extreme value distribution the data fall into. A shape parameter of $k = 0$ is a Type I extreme value distribution, $k > 0$ is Type II or Fréchet distribution, and $k < 0$ is Type III or Weibull distribution. For two out of four of the datasets, the shape parameter was not significantly different from 0 at the 95% confidence level. The other two datasets had negative shape parameters. These differences in k might indicate a change in mechanism that affects the shape of the distribution. We feel, however, that to make such a statement would mean to overinterpret our data. The second-best fit in all cases was the EV-I max distribution. In two of the datasets ($x_f = 0.167$ and 0.534) competing models came close in AIC value ($\Delta g_i^{AIC} = 5$) but are still considered to have less support. We therefore decided to fit an EV-I (max) distribution to all four experiments. Fit parameters are reported in Table 1 and Supporting Table 3.

x_f	Model	g^{AIC}	Δg^{AIC}	$\hat{J}$ or $\hat{J}_0$ (95% CI)	$\widehat{W'}$ (95% CI)	$\hat{\mu}$ (95% CI)	$\hat{k}$ (95% CI)
0.167	GEV	-1720	-1183	12.39 (11.35, 13.54)	-	1.901 (1.891, 1.912)	-0.2445 (-0.3004, -0.1885)
0.167	EV-I (max)	-537	0	12.44 (11.37, 13.50)	-	1.891 (1.881, 1.901)	-
0.167	Gompertz	-532	5	4.783e-10 (-4.598e-10, 1.416e-09)	-12.15 (-13.16, -11.14)	-	-
0.167	Gumbel/ EV-I (min)	-532	5	4.783e-10 (-4.598e-10, 1.416e-09)	-12.15 (-13.16, -11.14)	-	-
0.255	GEV	-1183	-760	14.95 (13.27, 16.84)	-	1.710 (1.699, 1.721)	0.004668 (-0.1066, 0.1160)
0.255	EV-I (max)	-423	0	14.92 (13.25, 16.59)	-	1.710 (1.700, 1.720)	-
0.255	Gompertz	-298	125	5.941e-07 (-2.744e-07, 1.463e-06)	-9.224 (-10.06, -8.392)	-	-
0.255	Gumbel/ EV-I (min)	-298	125	5.941e-07 (-2.744e-07, 1.463e-06)	-9.224 (-10.06, -8.392)	-	-
0.345	GEV	-1730	-1139	13.79 (12.56, 15.14)	-	1.498 (1.489, 1.508)	-0.05555 (-0.1382, 0.02712)
0.345	EV-I (max)	-591	0	13.98 (12.72, 15.24)	-	1.496 (1.487, 1.505)	-
0.345	Gompertz	-459	132	1.349e-06 (-3.259e-07, 3.025e-06)	-9.992 (-10.80, -9.188)	-	-
0.345	Gumbel/ EV-I (min)	-459	132	1.349e-06 (-3.259e-07, 3.024e-06)	-9.992 (-10.80, -9.188)	-	-
0.534	GEV	-2074	-1276	17.93 (16.49, 19.49)	-	1.273 (1.266, 1.280)	-0.2242 (-0.2679, -0.1806)
0.534	EV-I (max)	-798	0	18.03 (16.53, 19.53)	-	1.266 (1.259, 1.273)	-
0.534	Gompertz	-793	5	1.893e-09 (-1.399e-09, 5.186e-09)	-17.36 (-18.70, -16.02)	-	-
0.534	Gumbel/ EV-I (min)	-793	5	1.893e-09 (-1.399e-09, 5.186e-09)	-17.36 (-18.70, -16.02)	-	-

Supporting Table 3: Models, fit parameters, and goodness of fit for experiments with $x_f \geq 0.167$ M.

4.4 Dependence of Median Nucleation Time on Barium Concentration

The median nucleation time (half-life) was calculated for experiments with $x_f \geq 0.167$ M. The 95% confidence interval for the median nucleation time was calculated using the percentile bootstrap method as implemented in Matlab using the `bootci` function with 100,000 samples.[14] The median nucleation times were fit to the function $\tau_{0.5} = a \ln x_f + c$ using a non-linear least squares method with Matlab's built in `fit` function and the default trust-region algorithm.[14] The best fit coefficients with 95% confidence bounds are $\hat{a} = -0.55\ (-0.74, -0.35)$ and $\hat{c} = 0.96\ (0.71, 1.21)$.
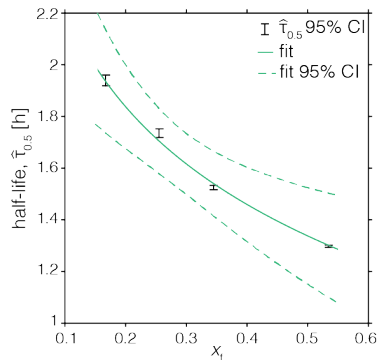
Supporting Figure 7. Plot of the empirical half-life, $\hat{\tau}_{0.5}$, i.e. the time at which at least one birefringent particle was observed in 50% of observed droplets, as a function of the barium cation fraction of the feed solution. Error bars indicate the 95% confidence interval, determined by bootstrapped percentile. A logarithmic model was fit to the data (solid line) and a 95% confidence interval for prediction was determined (dashed line).